Towards self-consistent simulation of radial effects on an axial PIC model of the Hall discharge

IEPC-2024-699

Presented at the 38th International Electric Propulsion Conference, Toulouse, France
June 23-28, 2024

Guillermo Cuerva-Lázaro*, Enrique Bello-Benítez†, Alberto Marín-Cebrián‡, and Eduardo Ahedo§
Department of Aerospace Engineering, Universidad Carlos III de Madrid, Leganés, Madrid, 28911, Spain

The computational demands of 3D kinetic modeling of a Hall Thruster discharge are significant, requiring substantial resources and often resulting in impractically long computation times. As a result, reduced-dimensionality codes are commonly employed, some incorporating the effects of the unmodeled dimension(s). In this work, we introduced a new model to study wall interactions in a PIC simulation. Our model moves electrons and ions radially by prescribing a radial potential profile that differentiates between presheath and infinitely thin sheath. Particle removal is determined based on their radial energy relative to the sheath potential, allowing for kinetic effects on plasma-wall interactions. As a proof of concept, we include this model in axial PIC simulations of a Hall thruster discharge, assessing its physical accuracy, comparing the results with similar axial-radial PIC simulations, and evaluating its robustness against numerical parameters. This new wall interaction model could, in the future, be coupled with axial-azimuthal PIC simulations serving as an effective middle ground between computationally expensive 3D kinetic modeling and traditional 2D axial-azimuthal PIC simulations.

*PhD student, Department of Aerospace Engineering, gcuerva@ing.uc3m.es
†PhD student, Department of Aerospace Engineering, ebello@ing.uc3m.es
‡PhD student, Department of Aerospace Engineering, almarinc@pa.uc3m.es
§Professor, Department of Aerospace Engineering, eahedo@ing.uc3m.es

Nomenclature

e = Fundamental charge
n_n = Neutral density
u_{zn} = Neutral average axial velocity
$\dot{m}$ = Neutral mass flow
T_n = Neutral temperature
$\dot{m}_{zi}$ = Axial ion flow
m_i = Ion mass
n_i = Ion density
T_i = Ion temperature
c_s = Ion sound velocity
u_{zn} = Ion axial velocity
u_{riQ} = Ion radial velocity at sheath edge
S_{prod} = Source term due to ionization
m_e = Electron mass
n_e = Electron density
T_e = Electron temperature
p_e = Electron pressure
E_r = Radial Electric field
B_m = Maximum magnetic field
ϕ_{sh} = Potential drop at the sheath
ϕ^*_{sh} = Theoretical potential drop at the sheath
$\delta\phi_{sh}$ = Perturbation of potential drop at the sheath
j^*_W = Theoretical wall current
j_W = Wall current density
I_W = Wall current
ϕ = Electric potential
ν_e = Effective electron collision frequency
α_{ano} = Anomalous coefficient
I_∞ = Plume current
V_d = Discharge voltage
I_d = Discharge current
r_W = Wall radius
L_r = Channel width
L_{ch} = Channel length
A = Channel cross-section
z_m = Location of maximum magnetic field
l_m = Exponential decay length of the magnetic field
$\tilde{c}$ = artificial capacitance
w_p = Particle weight
Δl = Grid size
Δt = Time-step
f_D = Augmentation factor
ϵ_0 = Vacuum permittivity
ω_{ce} = Electron cyclotron frequency
ν_e = Electron effective collision frequency
HET = Hall Effect Thruster
PIC = Particle-In-Cell
MCC = Monte Carlo Collision

I. Introduction

The 3D kinetic modeling of a Hall Thruster discharge requires extensive resources and sometimes unfeasible computation times. Extensive research has been carried out to use reduced 1D or 2D models[1,2] to effectively simulate the plasma discharge. However, these approaches can neglect important phenomena that occur in the non-simulated directions. Consequently, the introduction of a virtual dimension in PIC simulations has been frequently employed, particularly in azimuthal and radial-azimuthal simulations, where the axial dimension is added to dissipate the energy generated by the electric field.[1,3–6] Incorporating the radial dimension in axial or axial-azimuthal simulations is equally crucial, as walls act as sinks and sources of particles and plasma-wall interactions significantly influence the axial profiles of main plasma parameters. Furthermore, it contributes to expanding the range of numerically convergent solutions for Hall-type plasmas and operational characteristics.

Over the years, numerous attempts have been made to accurately model wall interactions in PIC models without solving the Poisson equation in the radial direction. The first attempts to model wall effects were conducted by Adam et al.[7] and Coche et al.[8] In both works, they considered electron-wall collisions within the thruster channel. Electrons with radial energy higher than a prescribed potential energy of 20 V are likely to undergo an isotropic elastic collision. In this approach, electrons are not removed from the simulation domain or lose any energy when they collide with the walls. A similar approach was recently taken by Yamashita et al.[9] in a 1D axial PIC simulation, but the energy of the electrons was reduced after the wall collision. Both approaches have limitations, as they do not involve the removal of particles by the wall, and walls affect exclusively electrons, neglecting ion recombination at walls.

Tavant,[10] was one of the first authors to propose a wall interaction model where particles are removed from the simulation domain. To avoid charge imbalances, flux equality at the wall was imposed by absorbing the same number of electrons and ions at each time step. The flux was based on the ion thermal velocity in the radial direction, with the most energetic electrons being removed from the simulation domain, while there was no specific ordering for the ions. Petronio[11,12] expanded on this approach, using a Bohm flux based on the ion sound velocity and stating that the density at the sheath edge was half of the bulk density. Although both approaches demonstrated a significant improvement over previous models, they require the ordering of electrons by their radial energy, which incurs substantial computational costs. Additionally, Petronio assumed a fixed ratio between the bulk plasma and the sheath, with flux to the walls derived from fluid theory. This simplification means that the presheath and sheath regions are not explicitly modeled, thereby neglecting the kinetic effects on plasma-wall interactions.

In this work, we propose an alternative model to study wall interactions in an axial PIC simulation. This new model differentiates between presheath and sheath regions, moves electrons and ions radially, and satisfies the dielectric condition at the walls by prescribing a radial potential profile, based on results from fluid and kinetic 2D axial-radial models. Consequently, there is no need for electron ordering, nor assumptions regarding the ratio between the plasma bulk and sheath edge. Instead, the ability of electrons to overcome the electric potential at the sheath depends on their radial energy. Lastly, with this model, it is possible to account for kinetic effects on plasma-wall interactions and analyze multiple wall quantities such as wall current densities, sheath potential drop, or depletion of electron radial velocity distribution function.

We demonstrate that this new wall-interaction model yields numerical solutions in a 1D axial PIC simulation that are highly similar to those from a 2D axial-radial PIC simulation performed with the same input parameters,[13] resolving the radial dimension self-consistently. Furthermore, the model exhibits high robustness against numerical parameters. These results represent a substantial improvement over the current state of the art and have major implications for including wall interactions in axial-azimuthal PIC simulations, where the interplay between wall interactions and kinetic instabilities has not been studied.

The kinetic model is presented in Section II, and the new model for wall interactions is discussed in Section III, in Section IV, we present the first axial PIC simulations of a Hall thruster discharge with wall effects, demonstrating its physical accuracy and robustness against numerical parameters.

II. Kinetic model

The in-house code PICASO[13–15] in its axial-azimuthal version has been employed for the full-PIC simulations of the Hall thruster presented in this work. PICASO is a 2D3V explicit momentum-preserving PIC code that uses the Boris algorithm[16] for moving and weighing electron and ion macroparticles with a

first-order cloud-in-cell shape function on a uniform rectangular mesh, and employs a bi-linear interpolation scheme to retrieve the electromagnetic fields acting on each particle. Poisson's equation is solved using a finite-difference solver that uses the PARDISO[17–19] direct solver in Intel MKL. Particle lists are split between different CPUs using a particle-decomposition parallelization with OpenMP. All the simulations shown in this paper were run in a workstation with 2 sockets, each one with 20 cores Intel(R) Xeon(R) Gold 6230 CPU @ 2.10GHz.

Electrons (e) and singly-charged ions (i) are simulated as two different particle populations with constant macroparticle weights. To avoid simulating time scales associated with the slow neutral dynamics, neutrals are described by a simple neutral depletion law that conserves the total mass flow[13]

$$n_n(z) = \frac{\dot{m} - \dot{m}_{zi}(z)}{A m_i u_{zn}}. \tag{1}$$

where m_i is the ion mass, A is the channel cross-section, u_{zn} is an average velocity of neutrals, $\dot{m}_{zi}$ is the axial ion flow on an axial constant surface and $\dot{m}$ is the injected neutral mass flow at the back wall.

The model assumes an external radial magnetic field that varies only in the axial direction given by

$$\mathbf{B}(z) = B_m \exp -\frac{(z - z_m)^2}{l_m^2} \mathbf{1_r}, \tag{2}$$

with $B_m = 250\ G$, $z_m = 2.5\ cm$, $l_m = 1.35\ cm$ for $z < z_m$, and $l_m = 1cm$ for $z > z_m$, shown in Figure 1.

To include radial wall interactions and test them, PICASO was reduced to simulate a 1D axial domain. Particles are tracked in 3D3V, and even though Poisson's is solved only in the axial direction, particles are also moved radially since a radial potential profile was imposed. Figure 1 provides a sketch of the simulation domain, consisting of the thruster channel and the near plume. Although the radial direction is depicted, it is not self-consistently resolved in any of the simulations presented in this paper. Nevertheless, it is important to show this direction to indicate the regions where ion and electron fluxes to the wall are expected. The electron emission from the cathode in our model differs from previous axial or axial-azimuthal Hall-thruster simulations,[7–9,11,12,20] which used a surface cathode to inject either the current collected at the anode or based on a quasineutrality condition in the cathode plane. Instead, we opted for a volumetric cathode,[21] 2mm in length, located near the end of our simulation domain (grey box in Figure 1). This volumetric cathode injects the current collected at the anode plane, sampled from a semi-Maxwellian VDF at 1 eV along the cathode's region of influence. The boundary surface on the right of our domain is treated as a free-loss zero-current boundary.

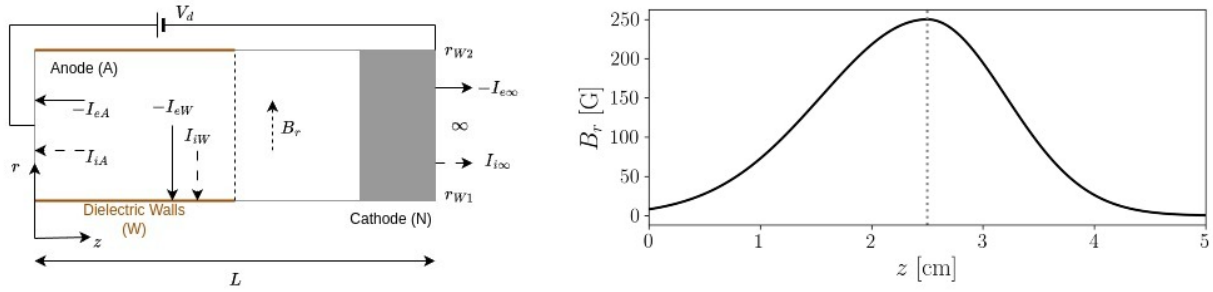

Figure 1. Simulation domain sketch with the applied magnetic field and arrows indicating the direction of the expected ion and electron fluxes. The grey regions in the domain refer to the volumetric cathode. The dotted vertical line in the magnetic field plot denotes the thruster exists.

The electric potential, ϕ, is self-consistently obtained from the Poisson equation, where we imposed Dirichlet boundary conditions at the anode and cathode. Ionization collisions are resolved using standard Monte Carlo Collision (MCC) algorithms, with a cross-section provided by the analytical model proposed by Drawin et al.[22] Ions are assumed collisionless. For electron momentum-transfer collisions, we use the crude model presented by Marín-Cebrián et al.[23] This model assumes virtual isotropic scattering collisions with an effective frequency, $\nu_e = \alpha_{ano}\omega_{ce} + \nu_{e0}$, where $\alpha_{ano} = 0.01$ is an anomalous transport coefficient, $\omega_{ce} = eB/m_e$ is the electron cyclotron frequency and $\nu_{e0} = 10^6 s^{-1}$.

Table 1 gives the values of the main physical parameters and magnitudes used throughout the different simulations presented in this paper. The values are chosen to be equal to the ones used by Marín-Cebrían et al.[13] The discharge voltage of the anode and cathode is $V_d = 300$ V while I_d is the discharge current.

Type	Symbol	Value	Units
Species settings			
Initial plasma density	$n_{e0} = n_{i0}$	4×10^{17}	m^{-3}
Initial ion temperature	T_{i0}	0.5	eV
Initial electron temperature	T_{e0}	10	eV
Reference neutral density	$\dot{m}/\left(m_i u_{zn} A\right)$	2×10^{19}	m^{-3}
Axial neutral velocity	u_{zn}	500	m/s
Neutral temperature	T_n	0.0	eV
Cathode emission temperature	T_{eNf}	1	eV
Physical system parameters			
Channel inner radius	r_{W1}	35	mm
Channel inner radius	r_{W2}	50	mm
Channel length	L_{ch}	25	mm
Domain length	L	50	mm
Anode potential	ϕ_A	300	V
Cathode potential	ϕ_C	0	V
Anode magnetic field	B_A	8	G
Maximum magnetic field	B_m	250	G
Surface interaction parameters			
Artificial Capacitance	$\tilde{c}$	2.5×10^{-5}	F/m^2

Table 1. Input parameters for the kinetic model

III. Treatment of the radial dimension

In addition to the movement of particles in the directions where Poisson's equation is solved, electrons and ions also move radially. Their radial movement is limited by the channel width, i.e. $L_r = r_{W2} - r_{W1}$. Following this approach, we encounter two main challenges.

First, we need to set the shape of the ambipolar electric field in the presheath, which will accelerate ions toward the wall ensuring the Bohm criterion at the sheath edge, while slowing down electrons. Second, we must model the sheath at walls, guaranteeing that the walls are dielectric, $j_W = 0$. Therefore, the model differentiates between a presheath and a sheath, prescribing an analytical expression for an electric radial field in the presheath and a potential drop in an infinitely thin sheath. Lastly, this model differentiates between the thruster channel and the plume. Therefore, we only consider particle absorption to the walls within the thruster channel, where we can obtain an approximate solution for both regions of our model.

A. Presheath

As we will not be solving Poisson's in the radial direction, we need to formulate an expression of the radial electric field that can vary in z, r. We have formulated an expression based on the ion's fluid momentum equation in the radial direction.

Considering steady state, neglecting cylindrical effects, cold ions, and assuming that ion's azimuthal velocity is smaller than the other velocities, $u_{\theta i} \ll u_{zi}, u_{ri}$, and solving for the electric radial field. The ion's fluid momentum equation in the radial direction can be expressed as

$$E_r = \frac{m_i}{e n_i}\left(n_i\left(\tilde{u_{ri}}\frac{\partial \tilde{u_{ri}}}{\partial r} + u_{zi}\frac{\partial \tilde{u_{ri}}}{\partial z}\right) + \tilde{u_{ri}} S_{prod}\right). \tag{3}$$

where m_i is the mass of the ion, n_i is the ion's density, u_{zi}, u_{ri} are the ion's axial and radial velocities, and S_{prod} is the source term due to the ionization of neutrals. Most of the quantities given in the equation above are calculated by PICASO. However, an analytical expression for the ion's radial velocity must be given, $\tilde{u_{ri}}$. Following Bohm criterion,[24] ions should reach the sheath edge with at least ion sound velocity. From previous axial-radial kinetic simulations,[13] the shape of the ion's radial velocity follows a cubic behavior, especially on the end of the radial domain. Consequently, we formulated a cubic profile on the ion's radial velocity such that

$$\tilde{u_{ri}}(z,r) = c_s(z)\left(\frac{r - r_M}{r_{W2} - r_M}\right)^3, \tag{4}$$

where $c_s(z) = \sqrt{\frac{T_e(z)}{m_i}}$ is the ion sound velocity. From Eq. (4), it is clear that our equation will depend on two dimensions, as the electron temperature varies axially throughout the chamber. The electric radial field is solely applied in the thruster channel, to ensure a smooth transition to the near plume, and an exponential decay is imposed. The model for the presheath is quite advantageous as the radial electric field is computed at the particle's radial position, and it solely depends on calculated quantities by PICASO.

B. Sheath

The sheath is modeled as an infinitely thin layer in our radial domain, $r_Q \sim r_W$. Consequently, when particles reach the wall boundaries, we must account for ions removed by the walls and electrons either removed or reflected based on their radial energy. Moreover, the dielectric condition at the wall, $j_W = 0$, should be satisfied in a steady state. We modeled the potential drop at the sheath as a sum of two contributions: the potential drop derived from the fluid formulation in the sheath,[24] ϕ^*_{sh}, and a small perturbation, $\delta\phi_{sh}$, that accounts for kinetic effects, and non-zero wall current in the transient state. Therefore, the expression is given by

$$\phi_{sh} = \phi^*_{sh} - \delta\phi_{sh} = \frac{T_e}{e}\ln\sqrt{\frac{m_i}{2\pi m_e}} - \delta\phi_{sh}. \tag{5}$$

During a transient state, the flux of different species to the wall might be unequal. To account for this, the perturbation time evolves following a capacitor-like behavior with a prescribed artificial capacitance, $\tilde{c}$. This relationship is described by

$$\frac{\partial(\delta\phi_{sh})}{\partial t} = \frac{j_{rW}}{\tilde{c}}, \tag{6}$$

where j_{rW} represents the current density of the wall. As it will be shown in section IV-B1, the artificial capacitance does not alter the solution and the perturbation contribution remains small compared to the main contribution from sheath theory, $\delta\phi_{sh} < \phi^*_{sh}$.

IV. 1Dz Results

As a proof of concept for introducing wall effects in PIC simulations, we begin with a 1Dz simulation of a Hall thruster discharge to evaluate the accuracy and convergence of this new wall algorithm. Additionally, we aim to test the algorithm's robustness against various numerical parameters, such as artificial capacitance, the initial number of particles per cell, and the augmentation factor on the electric permittivity, which also affects the grid size and time step.

A. Reference simulation

Based on the input parameters depicted in Table 1, we conducted the first PIC simulation with the numerical parameters provided in Table 2. The computation time for this simulation was approximately 4-5 hours.

Simulations start with equal particle densities $n_{e0} = n_{i0} = 4 \times 10^{17}$ with Maxwellian distributions with temperatures $T_{e0} = 10eV$ and $T_{i0} = 1eV$. Populating the domain with initially 40 macroparticles per cell, each macroparticle has a constant weight of $w_p = 1.64 \cdot 10^9$.

Figure 2 illustrates the temporal evolution of main wall quantities calculated by our wall algorithm. In a steady state, the currents to both walls satisfy the dielectric condition. Moreover, the potential drop at the sheath and its perturbation converge to a specific mean value, as well as satisfying that $\delta\phi_{sh} < \phi_{sh}$.

Numerical parameters	Symbol	Value	Units
Grid spacing	Δl	0.4	mm
Time-step	Δt	20	ps
Simulated time	t_{sim}	80	μs
Augmentation factor	f_D	20	
Initial number of particles per cell	N_{ppc}	40	

Table 2. Numerical parameters for the reference simulation.

By examining the time evolution of the wall currents, three distinctive regions can be identified. Initially, more electrons reach the wall due to their higher mobility. As time evolves, ions are accelerated to the wall by the ambipolar electric field. While electrons are slowed down and reflected by the sheath if their energy is not sufficient to overcome the potential difference. Consequently, there is a period when the ion flux to the walls exceeds the electron flux. Over time, the electron flux adjusts to match the ion flux, ultimately achieving a net zero wall current at around $t \sim 30\ \mu s$, dotted vertical line in Figure 2. Lastly, as our domain is planar and no cylindrical effects are considered, the wall quantities for the inner and outer radii are symmetric.

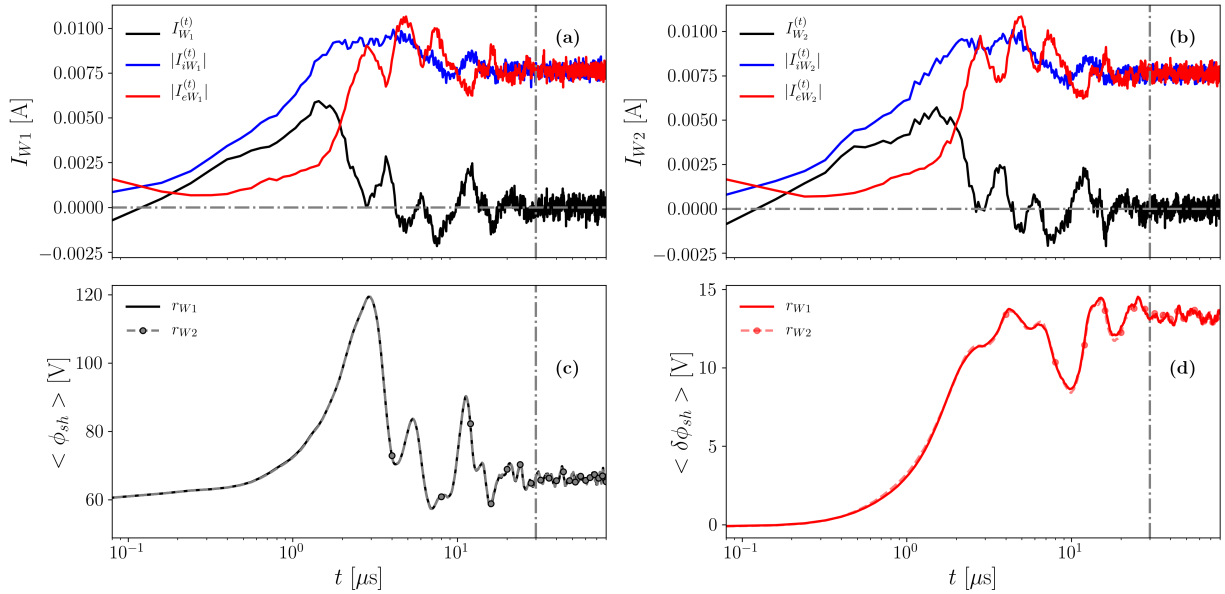

Figure 2. Time evolution of averaged wall quantities over the whole domain (a), (b) electron and ion currents to inner and outer walls, (c) potential drop in the sheath for inner and outer walls, and (d) perturbation in the potential drop for inner and outer walls. The vertical dotted line marks the time for achieving dielectric conditions.

Figure 3 depicts the temporal evolution of plasma currents to the anode (A), to the free loss boundary (∞) and discharge current (I_d). It also shows the contributions to the ion continuity equation over the whole simulation domain and the convergence of the mean electron density along with the average number of particles per cell.

Each subfigure in Figure 3 provides a key insight. The evolution of electron and ion currents indicates that we achieve a current-free plume, $I_\infty = 0$. In addition, the discharge current satisfies that $I_d = -I_{iA} - I_{eA}$. Examining the contributions to the ion continuity equation integrated over the whole domain. It can be observed that the production due to ionization is balanced by losses to the domain boundaries and the time-derivative term vanishes at steady conditions. Finally, the simulation converges as the mean density stabilizes after $t \sim 30\mu s$, dotted vertical line in Figure 3 (c). In a steady state, the average number of particles per cell remains constant, with 93 macroparticles per species, providing a good statistical representation.

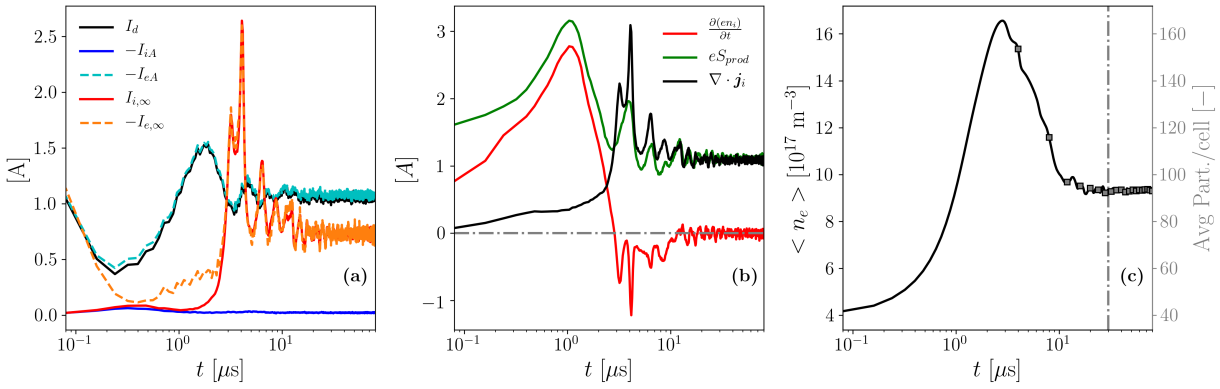

Figure 3. Time evolution of (a) electron and ion currents at the anode, discharge current, and currents at the end of the simulation domain, (b) contributions to the ion continuity balance integrated over the whole simulation domain, and (c) mean electron density and mean number of particles per cell. The dotted vertical line marks the time for achieving a steady-state solution.

Figures 4 - 7 illustrate the steady-state response of the plasma discharge. To reduce noise from the PIC simulation, all steady-state results shown below and in the next subsections correspond to a time average over the last 10 μs of the simulation.

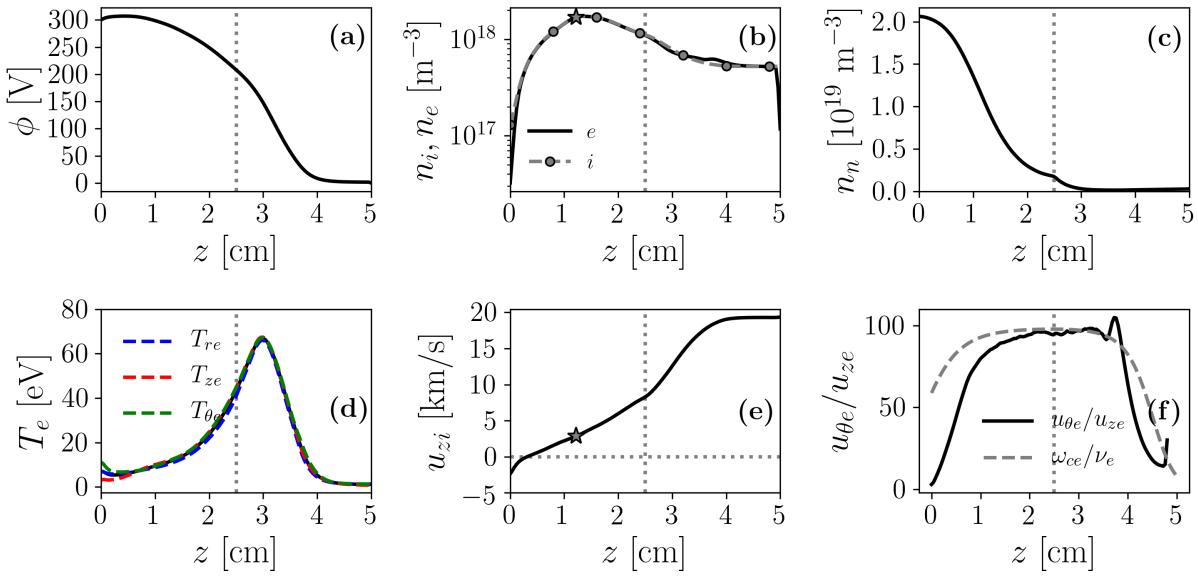

Figure 4. Axial profiles of relevant macroscopic variables: (a) electric potential, ϕ; (b) electron and ion particle densities, n_e and n_i respectively; (c) neutral particle density, n_n; (d) the ion axial velocity, u_{zi}; (e) electron average temperature, T_e, and the three diagonal components of $\bar{\bar{T}}_e$; and (f) the ratio between electrons azimuthal and axial velocity, $u_{\theta e}/u_{ze}$. Dotted vertical lines mark the thruster channel exit. Star markers show the location of the axial ion sonic point $u_{zi} = c_s$ with $c_s = \sqrt{T_e/m_i}$ the local sonic speed.

Figure 4 presents 1D axial profiles, which exhibit the expected trends of an axial discharge in a HET. The electric potential, $\phi(z)$, peaks around 307 V near the anode region and decreases to zero at the free loss boundary, located at $z = 5cm$. Consequently, ions accelerate axially until reaching the volumetric cathode region, with maximum plasma density near the ion sonic point. Plasma is quasi-neutral except near the anode and free loss boundary where sheaths form. Most ionization occurs inside the channel, depleting neutral density before the exit. Electrons are emitted from the cathode, heated to a maximum of 66 eV in the near plume, and then cool down due to ionization and wall losses inside the channel. Electron temperatures

are mostly isotropic, except near the anode.

Compared to an axial-radial kinetic simulation with the same input parameters,[13] there is a strong similarity in the axial profiles displayed in Figure 4, particularly in the electric potential, plasma density, ion's axial velocity profiles, and the ratio between azimuthal and axial electron velocities. Additionally, when comparing the ratio between azimuthal and axial electron velocities with the classical Hall parameter, ω_{ce}/ν_e, we observe the importance of finite Larmor radius effects (FLR) in the electron azimuthal equation, as seen in previous 1Dz PIC[9] and 2Dzr PIC[13] studies. Nevertheless, due to the omission of secondary electron emission, the axial PIC overestimates electron temperature and moves its peak further downstream. The introduction of secondary electron emission into this model is straightforward and will be addressed in future work.

Unlike previous simulations with wall effects,[7–10,12] our wall model not only modifies the axial profiles but also allows the analysis of key wall quantities such as wall current densities, ion's radial velocity at the sheath edge, the potential drop in the sheath, and the replenishment fraction. These can be compared with well-known fluid theory results to assess the accuracy of our wall algorithm, as displayed in Figure 5.

The theoretical wall current density is given by

$$j_W^* = en_{i,Q}\sqrt{\frac{T_e}{m_i}} \tag{7}$$

where $n_{i,Q}$ is the ion's density at the sheath which is calculated self-consistently in PICASO by surface weighting the ions exiting radially at each time iteration. The replenishment fraction is introduced to quantify non-Maxwellian effects on wall interaction parameters, previous works have defined it as the ratio between the kinetic electron current density to a wall W and a theoretical Maxwellian electron population. Assuming sonic ions and quasineutrality at the Debye sheath edge and disregarding secondary electron emission contributions, the sheath potential drop is given by

$$\phi_{sh} = \phi_{sh}^* + \frac{T_e}{e}\ln(\sigma_{rp}). \tag{8}$$

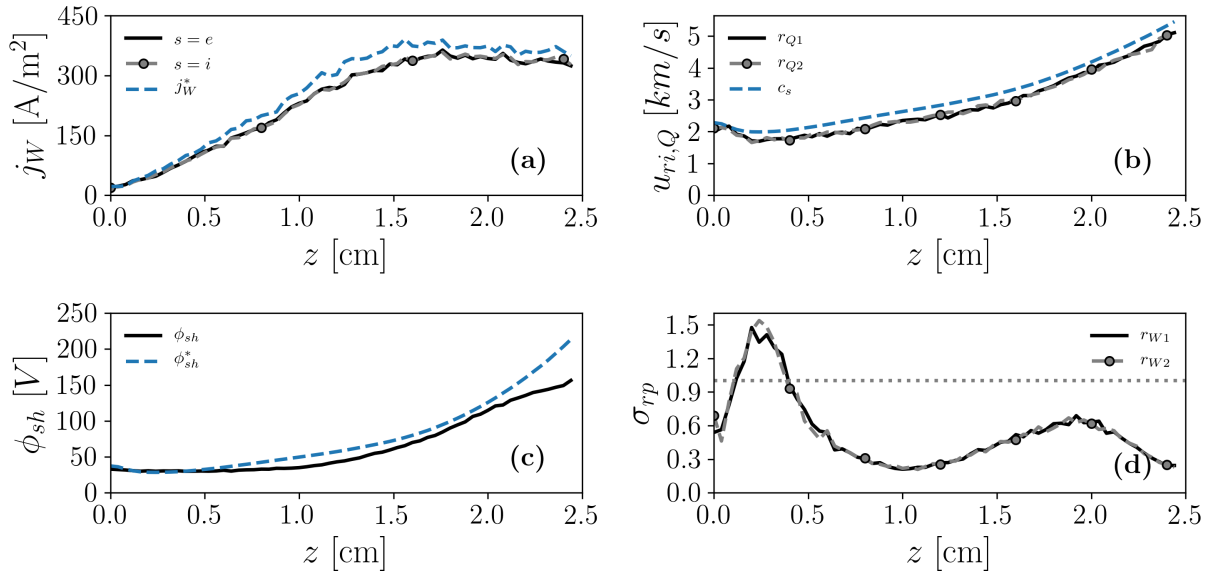

Figure 5. Axial profiles of relevant wall properties: (a) Wall current densities, j_W; (b) ion's velocity at the entrance of the sheath for both radii, $u_{ri,Q}$; (c) Potential drop at the sheath, ϕ_{sh}; (d) replenishment fraction, σ_{rp}.

Examining Figure 5 (a) - (b), it is evident that ions approach the sheath with velocities nearly matching the ion sound speed, and the ion and electron fluxes at steady state closely align with sheath theory predictions. The potential drop at the sheath generally follows the expected trend from sheath predictions.

However, deviations occur due to ions not precisely reaching sound speed and kinetic effects resulting from non-neutrality at the sheath edge. The replenishment fraction, depicted in Figure 5 (d), exhibits a trend consistent with previous axial-radial kinetic simulations.[13] It increases in the near anode region and stabilizes around 0.3 after $z > 1cm$.

Another important effect of the introduction of wall interactions is the depletion of the radial velocity distribution functions (VDFs). PICASO allows us to calculate the electron velocity distribution functions at several nodes of the simulation domain. Figure 6 depicts normalized 1D electron VDFs, $\hat{f_e}^{(r)}(v_r), \hat{f_e}^{(z)}(v_z)$, as well as the Maxwellian VDFs with the local T_e in logarithmic vertical scale, which are calculated at four axial positions within the chamber.

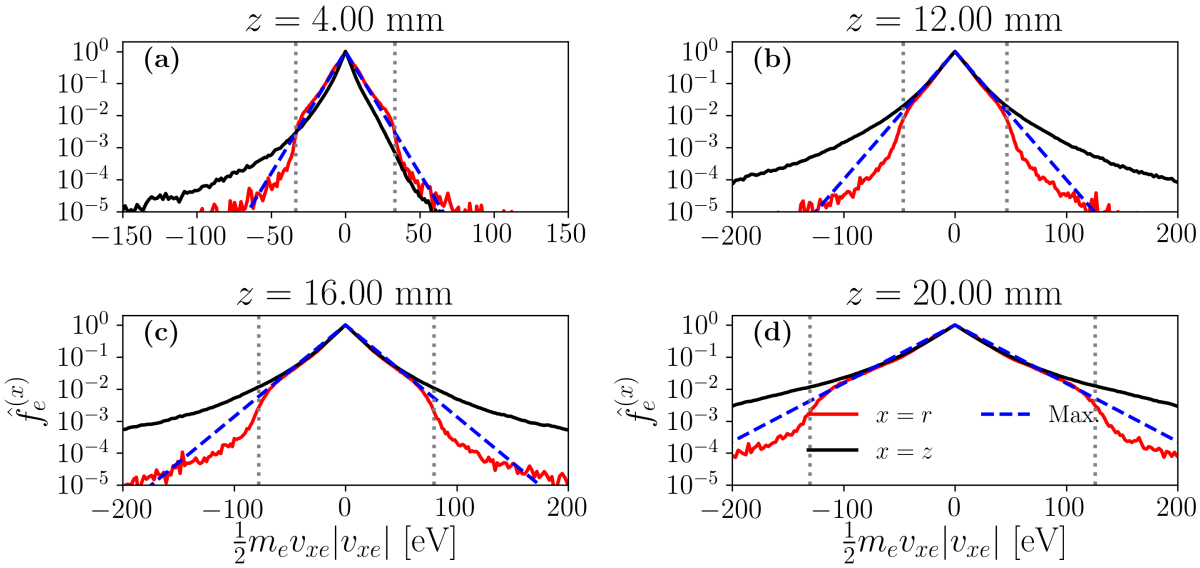

Figure 6. 1D normalized electron VDFs, $\hat{f_e}^{(r)}(v_r)$ (red) and $\hat{f_e}^{(z)}(v_z)$ (black), at four axial locations. Dashed blue lines represent a Maxwellian VDF at the local T_e. Vertical dotted lines mark $e\phi_{WM}$, i.e. the approximate wall-collection energy for $f_e^{(r)}(v_r)$.

Examining the radial VDFs at various locations within the chamber, we consistently observe depletion due to wall collection at energies corresponding to the potential drop between mid-radius and wall, $e\left(\phi_M - \phi_W\right)$. This reduction indicates that collisions are unable to replenish the high-energy tails, a behavior observed in prior studies employing axial-radial PIC simulations.[13] At the anode region, $z = 4\ mm$, axial and radial VDFs exhibit different slopes at low electron velocities. Furthermore, there is an asymmetry in the axial VDFS due to electron collection at the anode: the negative tail reflects electrons traveling to the anode and being collected there, resulting in asymmetry in the positive side of the VDF. Conversely, at axial locations in the middle and end of the channel $z = 12, 16, 20\ mm$, axial and radial VDFs are symmetric and at low electron velocities showing similar slopes and resembling a Maxwellian VDF.

To further assess the relevance of wall interactions, we can study the steady-state current balance for electrons and ions. In steady-state, electron and ion currents integrated over a radial section must satisfy[13]

$$\frac{dI_{zs}}{dz} = \frac{dI_{prod}}{dz} - \frac{dI_{rs}}{dz} \quad s = e, i \tag{9}$$

with I_{zs} the axial current, $\frac{dI_{prod}}{dz}$ the rate of current production, and $\frac{dI_{rs}}{dz}$ the rate of current losses to the wall. As walls are dielectric, $I_d = I_{ze} + I_{zi}$ must be satisfied. Figure 7 displays the different axial currents, as well as the three contributions to Eq. (9).

By examining Figure 7, it is evident that the PIC simulation satisfies the current balance described by Eq. (9) in a steady state. Similar results were observed by Marín-Cebrían et al.[13] and previous 1D analyses. As we move axially through the chamber, the wall current gradually increases as the electron density and temperature rise. The production current peaks as we reach the maximum density and decreases as the

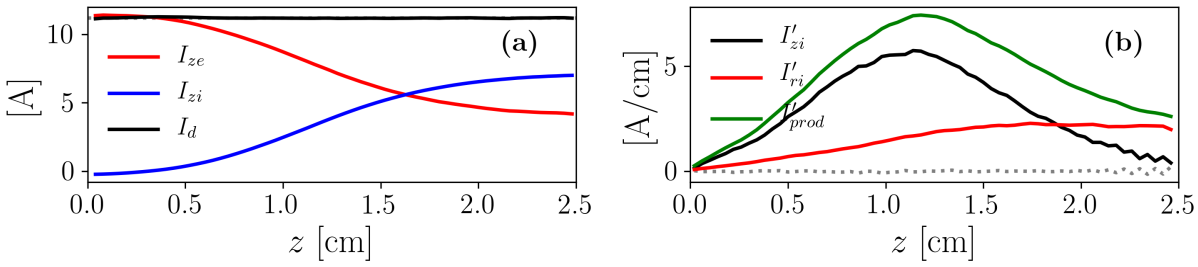

Figure 7. Current balance along the thruster channel: (a) axial electron and ion currents: and (b) current derivatives in Eq. (9) for the ion population. The notation $' \equiv d/dz$ is used in the legend.

neutral density depletes. At the thruster exit, the wall and production current are almost balanced. The dotted line in Figure 7 represents the sum of all three contributions from Eq. (9) which remains nearly zero across the entire channel.

B. Numerical robustness

Once a numerical solution has converged and the quantities obtained are physically meaningful and follow the expected trends previously obtained in the literature. It is essential to assess the solution's robustness to numerical parameters. The solution should exhibit negligible variation when numerical parameters are changed.

1. Artificial capacitance

While the plasma response might be different in the transient state for different values of the artificial capacitance, the steady state response should remain unaffected. To demonstrate this, we performed various simulations using the input parameters listed in Tables 1 and 2. In these simulations, we varied the artificial capacitance with values of $\tilde{c} = [250, 25, 2.5] \cdot 10^{-6}$. Figure 8 depicts axial profiles of the main macroscopic variables and wall quantities for different values of the artificial capacitance. It is important to mention that the artificial capacitance affects the transient time of the simulation. Consequently, the simulation with higher capacitance required longer simulation time to reach steady-state, $t_{sim} = 100\ \mu s$.

The black continuous line in Figure 8 represents the reference case described in section IV-A. The simulation results show no significant changes in macroscopic and wall variables for different values of artificial capacitance. Nevertheless, at lower capacitance values of $2.5 \cdot 10^{-6}$, slight variations are observed in the electron temperature and potential drop at the sheath compared to the reference case and higher capacitances. Despite these minor differences, the overall agreement remains very good.

2. Effects of doubling the initial number of particles per cell

Any PIC simulation should remain unaffected by the number of simulated macroparticles. Consequently, we performed three different simulations using the input parameters shown in Tables 1 and 2 for different initial numbers of particles per cell, $N_{ppc} = 20, 40, 80$. Note that these do not correspond to the average number of macroparticles at steady-state conditions. At steady state, the average number of macroparticles per cell for each of the cases is $N_{ppc,ss} \sim [50, 93, 182]$, for electrons and ions.

Figure 9 displays the axial profiles of the main macroscopic variables and wall quantities for different initial numbers of particles per cell, with the black continuous line being the reference case. There is a slight difference between the axial profiles for $N_{ppc} = 20$ compared with $N_{ppc} = 40, 80$. With a lower initial number of particles per cell, all quantities, macroscopic variables, and wall properties are slightly overestimated. However, there is no significant difference between $N_{ppc} = 40$ and $N_{ppc} = 80$, indicating that above a certain initial number of particles per cell, the steady-state response remains unaffected.

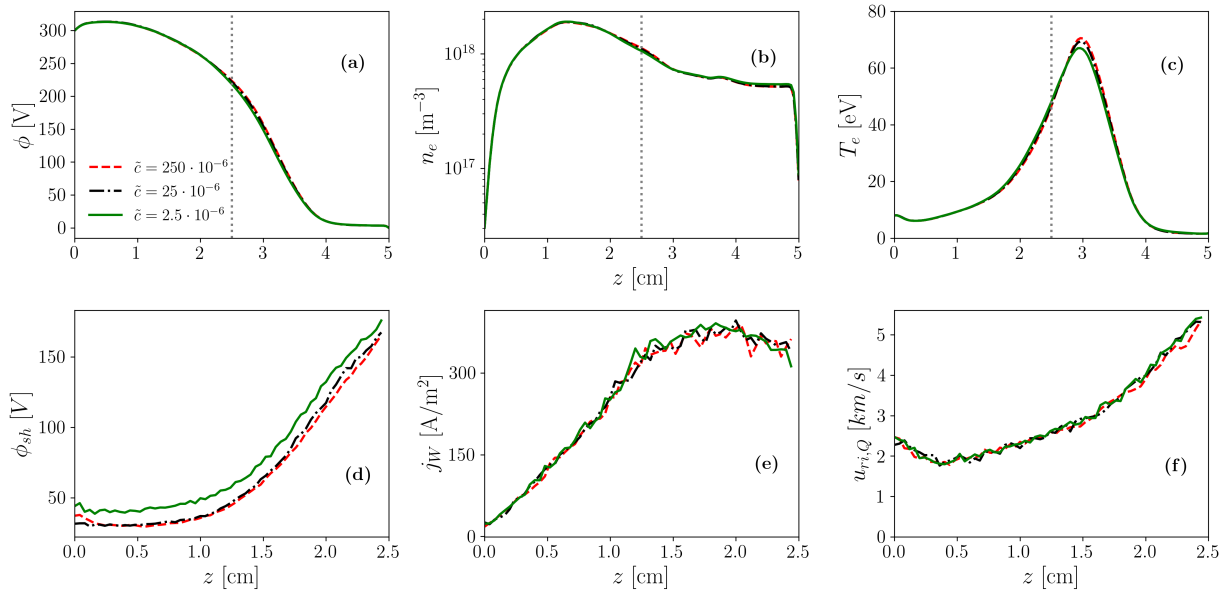

Figure 8. Axial profiles of relevant macroscopic variables and wall quantities for simulations with different artificial capacitance's $\tilde{c} = 2.5e-4, 1.25e-4, 2.5e-5, 5e-6, 2.5e-6$: (a) electric potential, ϕ; (b) electron particle density, n_e; (c) electron average temperature, T_e; (d) potential drop at the sheath, $\Delta\phi_{QW}$; (e) Wall current density, j_W; (f) ion's velocity at the entrance of the sheath, $u_{ri,Q}$. Dotted vertical lines mark the thruster channel exit.

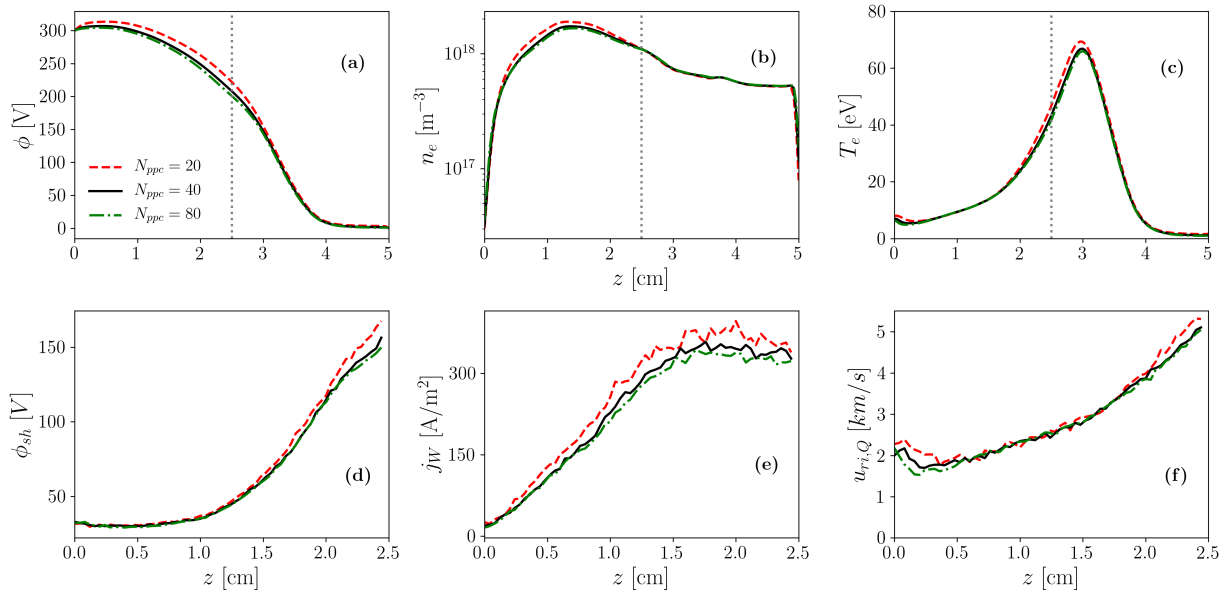

Figure 9. Axial profiles of relevant macroscopic variables and wall quantities for simulations with different initial number of particles per cell $N_{ppc} = 20, 40, 80$: (a) electric potential, ϕ; (b) electron particle density, n_e; (c) electron average temperature, T_e; (d) potential drop at the sheath, $\Delta\phi_{QW}$; (e) Wall current density, j_W; (f) ion's velocity at the entrance of the sheath, $u_{ri,Q}$. Dotted vertical lines mark the thruster channel exit.

3. Effects of changing the electric permittivity

Lastly, we have introduced an augmentation factor in the vacuum permittivity such that, $\epsilon = \epsilon_0 f_D^2$. This factor relaxes the numerical constraints imposed by the plasma frequency and Debye length. Values between

$f_D \sim 10 - 40$ have been used in previous PIC simulations.[13,25,26] The effect of this augmentation factor should not significantly affect the main axial profiles of the simulation, as long as the Debye length remains the smallest length scale of the problem. Consequently, we will compare the properties of the plasma discharge for different values of augmentation factor, $f_D = 10, 20$. It should be noted that for smaller values of f_D, the numerical constraints are stronger, necessitating finer grid sizes and smaller time steps. Consequently, the computational time increases from less than a day for $f_D = 20$, to around 4 days for $f_D = 10$. Simulations were run using the same physical input parameters given in Table 1, but for $f_D = 20$, the numerical parameters are given by Table 2, while for $f_D = 10$ the time-step and cell size have to be reduced a factor 2, as shown in Table 3.

Type	Symbol	Value	Units
Numerical parameters			
Grid spacing	Δl	0.2	mm
Time-step	Δt	10	ps
Simulated time	t_{sim}	80	μs
Augmentation factor	f_D	10	

Table 3. Numerical parameters for the effect of augmenting the electric permittivity.

Figure 10 presents axial profiles of key macroscopic variables and wall quantities for different values of the augmentation factor, f_D. We observe identical solutions except close the channel exit, where some differences can be found. For the solution with $f_D = 10$, a small bump in the electron density is observed at the channel exit. Consequently, we observed a similar bump in the electric potential at the channel exit which leads to an increase in electron temperature, resulting in a higher maximum electron temperature for $f_D = 10$. As a result, the potential drop at the sheath, which is influenced by the electron temperature profile, exhibits a mild difference between the two cases.

Overall, the changes in macroscopic variables and wall quantities between the augmentation factor of 10 and 20 are very mild, indicating a relatively minor impact of the augmentation factor on these profiles.

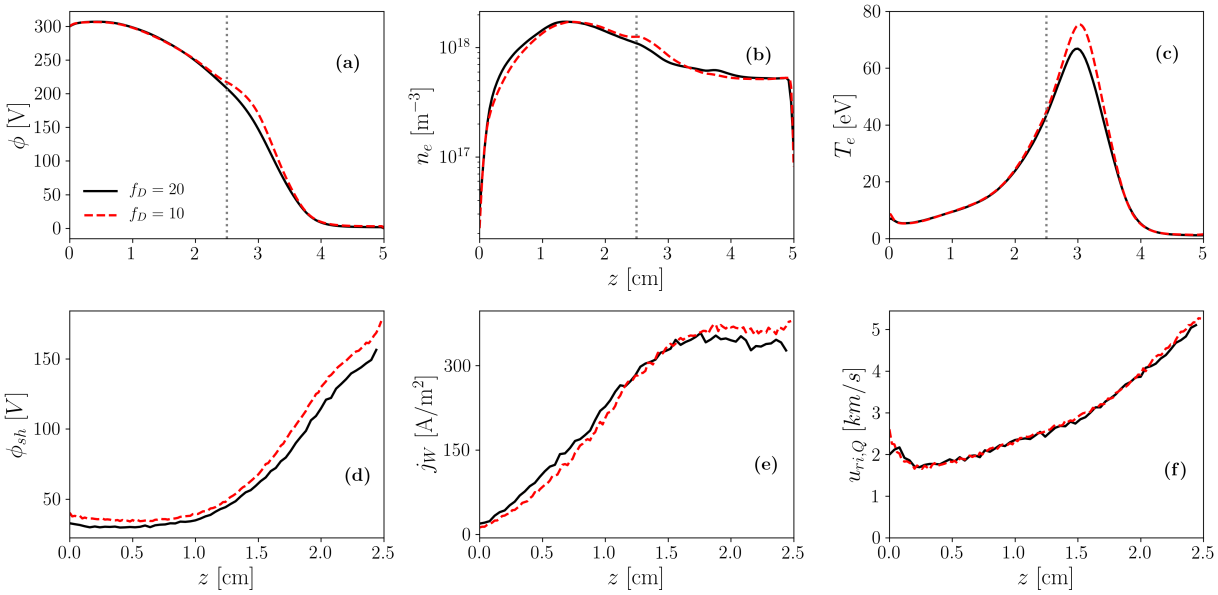

Figure 10. Axial profiles of relevant macroscopic variables and wall quantities for simulations with different augmentation factor $f_D = 20, 10$: (a) electric potential, ϕ; (b) electron particle density, n_e; (c) electron average temperature, T_e; (d) potential drop at the sheath, $\Delta\phi_{QW}$; (e) Wall current density, j_W; (f) ion's velocity at the entrance of the sheath, $u_{ri,Q}$. Dotted vertical lines mark the thruster channel exit.

V. Conclusion

In this article, we have proposed a new algorithm to account for wall interaction effects in PIC simulations that do not simulate the radial direction. Compared with previous efforts, this new approach can move particles in the radial direction, distinguish between presheath and sheath regions, kinetic effects are accounted for, and reach the dielectric condition at the walls in a steady state.

For the presheath, we formulated an expression for the ambipolar electric radial field based on the steady-state, planar ion's momentum radial equation, imposing a cubic radial profile on the ion's velocity that satisfies the Bohm criterion at the sheath edge. We considered an infinitely thin sheath and formulated an expression for the potential drop. This potential drop has two main contributions: a primary contribution from sheath theory and a small perturbation that accounts for kinetic effects and unequal wall fluxes in the transient state. This perturbation retains the memory of the flux of ions and electrons reaching the wall and achieves the dielectric conditions at the wall in the steady state. The simulation results show the expected trends in a HET discharge, the axial evolution of main macroscopic variables exhibits similar trends to an axial-radial PIC simulation with equal input parameters.[13] Wall quantities follow the trends predicted by sheath theory with small deviations due to kinetic effects. Electron velocity distribution functions inside the channel demonstrate the radial depletion due to wall collection at high energy tails. Inside the thruster channel, the walls reach the dielectric condition at steady state and the axial current balance is satisfied. The robustness of the simulation results has been validated by varying key numerical parameters, such as artificial capacitance, initial number of particles per cell, and augmentation factor.

The results of this paper demonstrate that including plasma-wall interactions is crucial in PIC simulations that do not self-consistently resolve the radial dimension. Wall interaction modifies the axial profiles and expands the range of numerically convergent simulations, as the same simulations without radial effects reach an unreasonable number of particles per cell threatening the numerical stability. A significant advantage of this model is its easy extrapolation to 2D axial-azimuthal simulations, a venue that will be explored in the future. This has major implications, as it allows us to study the coupling between kinetic instabilities and plasma-wall interactions. Additionally, it eliminates the need for an anomalous transport coefficient, as the 2D axial-azimuthal code can simulate azimuthal instabilities, which drive plasma turbulence and electron cross-field transport. Overall, a 2D axial-azimuthal PIC code with this wall interaction model would serve as an effective middle ground, bridging the gap between the extremely computationally expensive 3D kinetic modeling and traditional 2D PIC code, which neglects or oversimplifies the radial plasma dynamics. Consequently, we will explore the effects of this model on 2D axial-azimuthal PIC simulations in the future. Additionally, another branch of research will focus on improving the wall model to include secondary electron emission (SEE).

Acknowledgments

This work has been supported by the R&D project HEEP (PID2022-140035OB-I00) funded by MCIN/AEI/10.13039/501100011033 and by "ERDF A way of making Europe"

References

[1]Taccogna, F. and Garrigues, L., "Latest progress in Hall thrusters plasma modelling," *Reviews of Modern Plasma Physics*, Vol. 3, No. 1, 2019, pp. 12.

[2]Taccogna, F., Cichocki, F., Eremin, D., Fubiani, G., and Garrigues, L., "Plasma propulsion modeling with particle-based algorithms," *Journal of Applied Physics*, Vol. 134, No. 15, 10 2023, pp. 150901.

[3]Ducrocq, A., Adam, J., Héron, A., and Laval, G., "High-frequency electron drift instability in the cross-field configuration of Hall thrusters," *Physics of Plasmas*, Vol. 13, 2006, pp. 102111.

[4]Boeuf, J.-P., "Rotating structures in low temperature magnetized plasmas—insight from particle simulations," *Frontiers in Physics*, Vol. 2, 2014, pp. 74.

[5]Lafleur, T., Baalrud, S., and Chabert, P., "Theory for the anomalous electron transport in Hall effect thrusters. I. Insights from particle-in-cell simulations," *Physics of Plasmas*, Vol. 23, 2016, pp. 053502.

[6]Tavant, A., Croes, V., Lucken, R., Lafleur, T., Bourdon, A., and Chabert, P., "The effects of secondary electron emission on plasma sheath characteristics and electron transport in an discharge via kinetic simulations," *Plasma Sources Science and Technology*, Vol. 27, No. 12, 2018, pp. 124001.

[7]Adam, J., Herón, A., and Laval, G., "Study of stationary plasma thrusters using two-dimensional fully kinetic simulations," *Physics of Plasmas*, Vol. 11, 2004, pp. 295–305.

[8]Coche, P. and Garrigues, L., "A two-dimensional (azimuthal-axial) particle-in-cell model of a hall thruster," *Physics of Plasmas*, Vol. 21, 2014, pp. 023503.

[9]Yamashita, Y., Lau, R., and Hara, K., "Inertial and anisotropic pressure effects on cross-field electron transport in low-temperature magnetized plasmas," *Journal of Physics D: Applied Physics*, 2023.

[10]Tavant, A., *Study of the plasma/wall interaction and erosion on a plasma thurster of low power.*, Phd thesis, Université Paris Saclay, 2019.

[11]Petronio, F., Charoy, T., Alvarez Laguna, A., Bourdon, A., and Chabert, P., "Two-dimensional effects on electrostatic instabilities in Hall thrusters. I. Insights from particle-in-cell simulations and two-point power spectral density reconstruction techniques," *Physics of Plasmas*, Vol. 30, No. 1, 2023.

[12]Petronio, F., *Plasma instabilities in Hall Thrusters: a theoretical and numerical study*, Ph.D. thesis, Institut Polytechnique de Paris, 2023.

[13]Marín-Cebrián, A., Bello-Benítez, E., Domínguez-Vázquez, A., and Ahedo, E., "Non-Maxwellian electron effects on the macroscopic response of a Hall thruster discharge from an axial–radial kinetic model," *Plasma Sources Science and Technology*, Vol. 33, No. 2, feb 2024, pp. 025008.

[14]Bello-Benítez, E., Marín-Cebrián, A., Ramos, J. J., and Ahedo, E., "Two-dimensional kinetic simulation of electrostatic instabilities in a Hall plasma," 37^{th} *International Electric Propulsion Conference*, No. IEPC-2022-314, Electric Rocket Propulsion Society, Boston, MA, June 19-23, 2022.

[15]Bello-Benítez, E., Marín-Cebrián, A., and Ahedo, E., "Effect of injection conditions on the non-linear behavior of the ECDI and related turbulent transport," 2024, Available at `https://arxiv.org/pdf/2405.08761`.

[16]Birdsall, C. K., "Particle-in-cell charged-particle simulations, plus Monte Carlo collisions with neutral atoms, PIC-MCC," *IEEE Transactions on plasma science*, Vol. 19, No. 2, 1991, pp. 65–85.

[17]Alappat, C., Basermann, A., Bishop, A. R., Fehske, H., Hager, G., Schenk, O., Thies, J., and Wellein, G., "A recursive algebraic coloring technique for hardware-efficient symmetric sparse matrix-vector multiplication," *ACM Transactions on Parallel Computing (TOPC)*, Vol. 7, No. 3, 2020, pp. 1–37.

[18]Bollhöfer, M., Eftekhari, A., Scheidegger, S., and Schenk, O., "Large-scale Sparse Inverse Covariance Matrix Estimation," *SIAM Journal on Scientific Computing*, Vol. 41, No. 1, 2019, pp. A380–A401.

[19]Bollhöfer, M., Schenk, O., Janalik, R., Hamm, S., and Gullapalli, K., "State-of-the-Art Sparse Direct Solvers," *Parallel Algorithms in Computational Science and Engineering*, Springer International Publishing, 2020, pp. 3–33.

[20]Lafleur, T. and Chabert, P., "The role of instability-enhanced friction on 'anomalous' electron and ion transport in Hall-effect thrusters," *Plasma Sources Science and Technology*, Vol. 27, 2017, pp. 015003.

[21]Matyash, K., Schneider, R., Mutzke, A., Kalentev, O., Taccogna, F., Koch, N., and Schirra, M., "Kinetic simulations of SPT and HEMP thrusters including the near-field plume region," *IEEE Transactions on Plasma Science*, Vol. 38, No. 9, 2010, pp. 2274–2280.

[22]Drawin, H.-W., "Formular representation of the ionization cross section with respect to electron collision," *European Physical Journal. A*, Vol. 164, No. 5, 1961.

[23]Marín-Cebrián, A., Domínguez-Vázquez, A., Fajardo, P., and Ahedo, E., "Macroscopic plasma analysis from 1D-radial kinetic results of a Hall thruster discharge," *Plasma Sources Science and Technology*, Vol. 30, No. 11, November 2021, pp. 115011.

[24]Bittencourt, J., *Fundamentals of plasma physics*, Springer, Berlin, Germany, 2004.

[25]Szabo, J., Warner, N., Martinez-Sanchez, M., and Batishchev, O., "Full particle-in-cell simulation methodology for axisymmetric Hall effect thrusters," *Journal of Propulsion and Power*, Vol. 30, No. 1, 2014, pp. 197–208.

[26]Yuan, T., Ren, J., Zhou, J., Zhang, Z., Wang, Y., and Tang, H., "The effects of numerical acceleration techniques on PIC-MCC simulations of ion thrusters," *AIP Advances*, Vol. 10, No. 4, 2020, pp. 045115.